JOURNAL OF AIRCRAFT
Vol. 29, No. 2, March–April 1992

Navier-Stokes Study of Supersonic Cavity Flowfield with Passive Control

I. Kim* and N. Chokani†
North Carolina State University, Raleigh, North Carolina 27695

A computational investigation of the supersonic turbulent flow past a two-dimensional rectangular cavity with passive venting is described. The effect of passive venting was included through the use of a porous surface over a vent chamber in the floor of the cavity. The passive venting was numerically simulated by the use of a linear form of the Darcy pressure-velocity law. The time-accurate solutions of the two-dimensional, Reynolds-averaged, Navier-Stokes equations were generated using the explicit MacCormack scheme. The capability of the numerical scheme is first demonstrated by the computations of an *open* and *closed* cavity without passive venting. The results of these computations also provide a reference case for the passive venting computations. The effect of passive venting on the *closed* cavity is then demonstrated and analyzed. These results show that the passive venting dramatically changes the *closed* cavity flow to nearly an *open* cavity flow. The free shear layer formed between the high-speed outer flow and slower inner flow is seen to bridge the cavity completely, resulting in an *open* cavity flow. The passive venting velocities are determined to be less than 5% of the freestream velocities, and largely confined to the upstream and downstream portions of the cavity floor. The computational results show good agreement with available experimental data.

Nomenclature

C_D = drag coefficient, $\int_0^D (p_{RW} - p_{FW})\, dy/(\frac{1}{2}\rho_\infty u_\infty^2 D)$
CF = cavity floor
C_p = pressure coefficient, $(p - p_\infty)/(\frac{1}{2}\rho_\infty u_\infty^2)$
D = depth of cavity
D_v = Van Driest damping coefficient
E_0 = stagnation energy
e = specific internal energy
FP = flat plate upstream of cavity
FW = forward wall of cavity
I.P. = injection parameter, $(\rho_w v_w)/(\rho_\infty u_\infty)$
k_l = van Kármán constant
L = length of the cavity
L/D = length-to-depth ratio of cavity
M = Mach number
Pr = Prandtl number
p = static pressure
q = heat flux
R = specific gas constant
Re = freestream Reynolds number
RP = flat plate downstream of cavity
RW = rearward wall of cavity
T = temperature
T_c = characteristic time, inch/u_∞
u, v = velocity components in Cartesian coordinates
u_τ = friction velocity, $\sqrt{\tau_w/\rho_w}$
v_w = normal velocity of fluid injected or withdrawn from the cavity floor
v_w^+ = v_w/u_τ
x, y = Cartesian coordinates
y^+ = law-of-the-wall coordinate, yu_τ/ν
β = intermittency
δ = shear-layer thickness
μ = coefficient of molecular viscosity
μ_t = coefficient of eddy viscosity
ν = kinematic viscosity
ξ, η = transformed coordinates
ρ = density
τ = viscous stress

Subscripts
c = vent chamber condition
max = maximum value
min = minimum value
0 = stagnation condition
uc = cavity upstream corner condition
w = wall condition
$w+1$ = condition at grid point adjacent to wall
∞ = freestream condition

Received June 28, 1990; presented as Paper 90-3101 at the AIAA 8th Applied Aerodynamics Conference, Portland, OR, Aug. 20–22, 1990; revision received Feb. 12, 1991; accepted for publication Feb. 12, 1991.

*Graduate Research Assistant, Department of Mechanical and Aerospace Engineering.
†Assistant Professor, Department of Mechanical and Aerospace Engineering. Member AIAA.

Introduction

THE weapon bays on high-speed military aircraft and the recessed areas on some missile configurations are three-dimensional rectangular cavities. These features on the aerodynamic vehicle may have an adverse effect on the overall vehicle performance. Previous studies have shown that a supersonic flow over a cavity can exist in two distinct configurations. The first type of distinct flow is termed a *closed* cavity flow and occurs when the length-to-depth ratio is large (typically $L/D > 13$. In this flow, the shear layer, formed between the high-speed external flow and low-speed flow within the cavity, first turns towards the floor as it expands over the forward wall; an expansion fan is thus generated at the leading edge of the cavity. This shear layer then impinges on the cavity floor, and then turns upwards generating a series of compression waves. The shear layer then exits the cavity above the rearward wall. The typical surface pressure distribution associated with this flow is shown in Fig. 1, and consists of a low pressure over the upstream portion of the cavity floor, followed by a gradual pressure rise as the flow impinges on the cavity floor, a pressure plateau as the flow passes along the cavity floor, and a sharp pressure rise near the rearward wall. The second type of distinct flow is termed an *open* cavity flow and occurs when the length-to-depth ratio is small (typ-

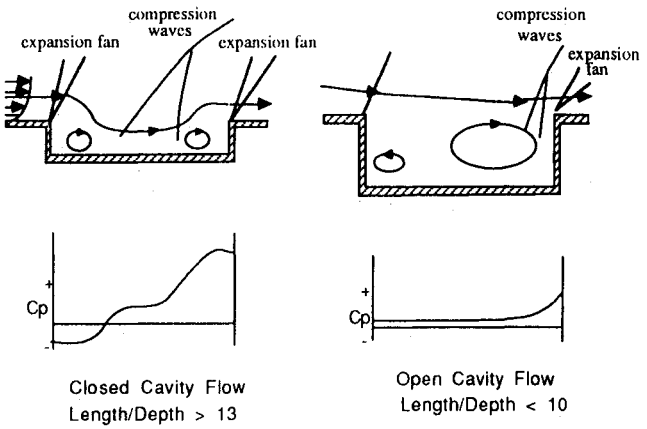

Fig. 1 Sketches of cavity flowfield characteristics.

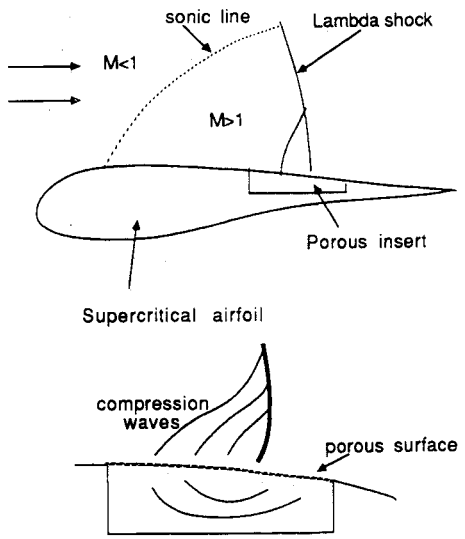

Fig. 2 Passive control on supercritical airfoil.

ically $L/D < 10$). In this flow the shear layer bridges the cavity entirely and impinges the rearward wall at the top. The associated pressure distribution is quite constant over most of the cavity length, and rises sharply at the shear layer impingement location on the rearward wall. Existing experimental data[1-2] has shown that the drag of a cavity with *closed* flow is substantially higher than that of a cavity with *open* flow. Therefore, it is desirable to have a cavity with *open* flow in practical aerodynamic applications. However, a cavity of small length-to-depth ratio is cumbersome for practical applications, and thus *closed* cavities are often employed.

Recently, the passive-control concept has been studied as an economical method to improve the performance of a supercritical airfoil[3-7] in transonic flows. This concept consists of replacing a part of the airfoil upper surface by a porous plate with vent chamber beneath the porous plate (Fig. 2). Since the pressure behind the shock is greater than the pressure in front of the shock, by locating the vent chamber in the shock foot region, flow suction and blowing can be achieved across the porous plate. In a supercritical airfoil, the blowing process produces a thickening of the boundary layer in front of the shock, and this thickening in turn generates a series of compression waves that weaken the nearly normal shock. In this manner the entropy rise across the shock is minimized, hence a smaller wave drag is achieved, and the drag rise Mach number is postponed. Recent experimental work conducted by Wilcox[2] has suggested that the passive-control concept can also be used to obtain more favorable pressure drag characteristics of the *closed* cavity flowfield. Wilcox's cavity model was designed to house a porous floor with a vent chamber

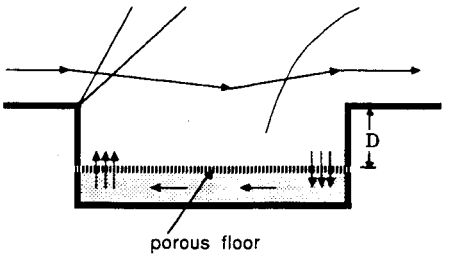

Fig. 3 Flowfield characteristics of cavity with passive control.

beneath the floor. For the *closed* cavity flow, this arrangement allowed the high pressure air at the rear of the cavity to vent to the low-pressure region at the front of the cavity and, it is suggested, caused the flowfield to switch to a nearly *open* flow (Fig. 3). Because of this change of the flow characteristics, the experimentally measured drag of *closed* flow cavities with passive control was reduced by a factor of 3. This motivated the development of a numerical method to computationally simulate the passive control effect on a supersonic cavity flowfield, with a view to complement the experimental investigations and to improve the understanding of the control concept.

Mathematical Formulation

Although a three-dimensional analysis is feasible, the cost of such an analysis for the initial studies would be extremely high. Previous studies[8] have nevertheless shown that the fundamental cavity flow is two-dimensional in nature. Thus for this study a two-dimensional analysis was chosen. The governing equations of the flow are the Reynolds-averaged, two-dimensional, unsteady, compressible Navier-Stokes equations. The conservation form of the equations written with respect to a Cartesian coordinate system are:

$$\frac{\partial U}{\partial t} + \frac{\partial E}{\partial x} + \frac{\partial F}{\partial y} = 0 \tag{1}$$

where U, E, and F are the following vectors:

$$U = \begin{bmatrix} \rho \\ \rho u \\ \rho v \\ E_0 \end{bmatrix} \tag{2}$$

$$E = \begin{bmatrix} \rho u \\ \rho u^2 + p - \tau_{xx} \\ \rho uv - \tau_{xy} \\ (E_0 + p)u - u\tau_{xx} - v\tau_{xy} + q_x \end{bmatrix} \tag{3}$$

$$F = \begin{bmatrix} \rho v \\ \rho uv - \tau_{xy} \\ \rho v^2 + p - \tau_{yy} \\ (E_0 + p)v - u\tau_{xy} - v\tau_{yy} + q_y \end{bmatrix} \tag{4}$$

$$\tau_{xx} = \frac{2}{3}(\mu + \mu_t)\left(2\frac{\partial u}{\partial x} - \frac{\partial v}{\partial y}\right) \tag{5}$$

$$\tau_{yy} = \frac{2}{3}(\mu + \mu_t)\left(2\frac{\partial v}{\partial y} - \frac{\partial u}{\partial x}\right) \tag{6}$$

$$\tau_{xy} = \tau_{yx} = (\mu + \mu_t)\left(\frac{\partial u}{\partial y} - \frac{\partial v}{\partial x}\right) \tag{7}$$

$$q_x = c_p\left(\frac{\mu}{Pr} + \frac{\mu_t}{Pr_t}\right)\frac{\partial T}{\partial x} \tag{8}$$

$$q_y = c_p\left(\frac{\mu}{Pr} + \frac{\mu_t}{Pr_t}\right)\frac{\partial T}{\partial y} \tag{9}$$

$$E_0 = \rho\left(e + \frac{u^2 + v^2}{2}\right) \tag{10}$$

Sutherland's expression for the molecular viscosity:

$$\mu = \mu_{\text{ref}}\left(\frac{T}{T_{\text{ref}}}\right)^{3/2}\frac{T_{\text{ref}} + S}{T + S} \tag{11}$$

where μ_{ref}, T_{ref}, and S are constants for air, T is the static temperature, and the perfect gas relationship:

$$p = \rho RT \tag{12}$$

are also employed. The effects of turbulence in the unsteady flow were accounted for by specifying a turbulent Prandtl number $Pr_t = 0.9$, and by incorporating the two-layer algebraic eddy-viscosity model of Cebeci and Smith with modifications for mass-transfer, free shear-layer flow and history effects. In the inner layer, the eddy-viscosity coefficient is given as:

$$\mu_{it} = \rho k_l^2 y^2 D_v^2 |u_y| \tag{13}$$

where k_l is 0.4 and D_v is the Van Driest damping coefficient with mass-transfer modification:

$$D_v = 1 - \exp[-y(|\tau_w/\rho_w|)^{1/2}/A\nu_w] \tag{14}$$

$$A = 26\exp(-5.9\, v_w^+) \tag{15}$$

On solid surfaces this reduces to the unaltered inner-layer formulation. This modification was previously used by Chokani and Squire[3] in numerical studies of passive control. In the outer layer over the flat-plate regions upstream and downstream of the cavity, the eddy-viscosity was given as:

$$\mu_{ot} = k\rho u_{\max}\theta_i\beta \tag{16}$$

where $k = 0.0216$ and $\beta = [1 + 5.5\,(y/\delta)^6]^{-1}$.

In the outer layer over the cavity floor, the free shear-layer flow modification[9] was used, and the eddy-viscosity can be expressed as:

$$\mu_{ot} = k'\rho u_{\max}\theta_i\beta \tag{17}$$

where $k' = 0.064$ and the incompressible momentum thickness is:

$$\theta_i = \int_0^\infty \left(1 - \frac{u}{u_{\max}}\right)\frac{u}{u_{\max}}\,dy \tag{18}$$

The eddy viscosity was switched from the inner to the outer value when $\mu_i > \mu_0$. A relaxation length modification[10] was applied to the eddy-viscosity obtained in the region over the cavity floor. This modification was incorporated to account for the strong disturbances the flow might encounter at the leading edge of the cavity, and is given as:

$$\mu_t = \mu_{uc} + (\mu_t - \mu_{uc})[1 - \exp(-(x - x_{uc})/10\delta)] \tag{19}$$

Here μ_t is the value calculated from Eqs. (13) and (17), μ_{uc} is the value at upstream corner, δ is instantaneous boundary-layer thickness at the upstream corner, and $(x - x_{uc})$ is the streamwise distance from the corner.

On all solid boundaries, the isothermal, no-slip conditions and zeroth-order linear extrapolation for pressure are used, which are

$$u = v = 0 \tag{20}$$

$$T = T_w \tag{21}$$

$$\frac{\partial p}{\partial n} = 0, \qquad \text{i.e. } p_w = p_{w+1} \tag{22}$$

where n is the direction normal to the surface. The isothermal wall temperature was taken as 510 R.

In simulating the flow on the porous surface, the normal wall velocity over the porous surface was evaluated using the linear form of the Darcy pressure-velocity law:

$$v_w = \frac{\sigma}{\rho_\infty u_\infty}(p_c - p_{w+1}) \tag{23}$$

where p_c is the vent chamber pressure and is taken from experimental data.[2] The geometric porosity factor σ for the 11.2% porosity of the porous cavity floor was taken as 0.607; this value was determined from interpolation of the experimentally determined values of Chokani and Squire[3] for 13.6% porosity and Savu et al.[4] for 10% porosity. The boundary condition given by the Eq. (23) was applied all along the porous cavity floor; no separate numerical solution of the vent chamber was thus necessary. This relationship was successfully used by Chokani and Squire[3] to simulate the transpiration velocity in a transonic shock-wave/boundary-layer interaction. An initial velocity profile based on the one-seventh power law is given along the upstream boundary, and the initial temperature profile is obtained from Crocco's temperature-velocity relation. This inflow boundary was more than ten mean boundary-layer thicknesses upstream of the cavity forward wall for all the computations; it is expected that this was sufficiently far upstream to be uninfluenced by the cavity flowfield phenomena. The outflow boundary and upper flow boundary were also positioned so that they did not influence the cavity flow significantly; at these locations the boundary conditions were determined by extrapolating the values from interior points.

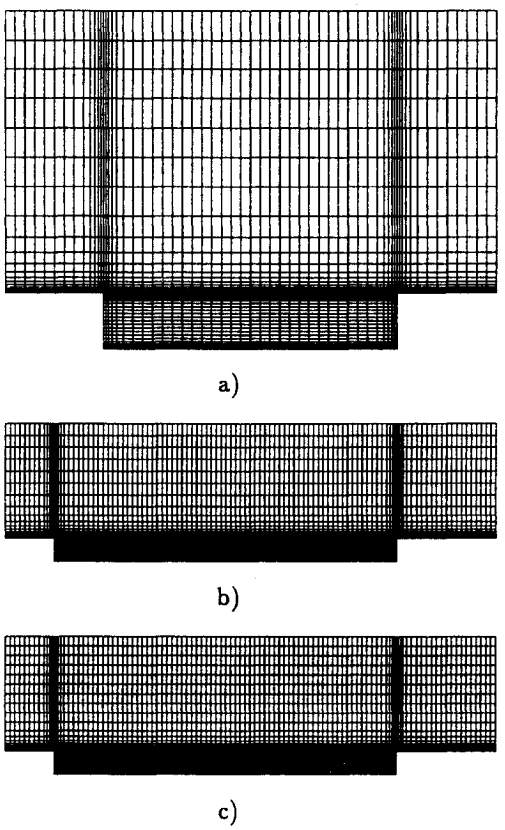

Fig. 4 Computational meshes: a) *open* cavity; b) *closed* cavity; and c) *closed* cavity with passive control.

Table 1 Flow conditions and cavity dimensions

M_∞	Re/ft	T_0, °R	L/D	D, in.	Cavity type
1.5	2×10^6	585	6	1.0	*Open*
1.6	2×10^6	585	17.5	0.4	*Closed*
1.6	2×10^6	585	17.5	0.4	*Closed* with passive control

Numerical Procedure

The computational domains surrounding the cavity configurations were described by nonuniform Cartesian grids shown in Fig. 4. The cavity dimensions are given in Table 1. In the *open* cavity flow, the grid in the planes exterior to the cavity and interior to the cavity consisted of 63 × 27 and 37 × 37 points, respectively, in the x, y directions; for the *closed* cavity the distribution of points was 113 × 27 and 77 × 37, respectively; for the *closed* cavity with passive control, it was 113 × 27 and 77 × 24. The clustering of grid points was determined so as to provide an adequate resolution of the flow features. Thus, grid clustering was used on the flat plates upstream and downstream of the cavity, along the cavity forward and rearward walls, and over the cavity mouth with the following minimum grid spacings:

$$(\Delta x_{\min}/D) = 0.05, \qquad (\Delta y_{\min}/D) = 0.0015 \quad (24)$$

Above the level of the cavity mouth, the grid was exponentially stretched towards the upper boundary. For the cavity flows without passive control, within the cavity the grids were exponentially stretched both from the cavity mouth and the cavity floor. In the case of the cavity flow with passive control, the computational results early in the study showed that there were no large flow gradients normal to the floor of the cavity, and so only stretching downwards from the cavity mouth was employed. On the flat plate upstream of the cavity, the normal grid spacing resulted in a $y^+ = 3$ and 7 at the first grid point above the plate at the inflow boundary for the *closed* and *open* cavity, respectively; the boundary layer, on the flat plate upstream of the cavity, had 16 and 13 points within it for the *closed* and *open* cavity flows, respectively. It was considered that the grids with these characteristics adequately captured the essential flow features. Conventional formulae were used to evaluate the metric coefficients of the transformation from the physical domain (x, y) to the uniform computational domain (ξ, η), i.e., central differences for the interior grid points and one-sided differences at all walls and flow boundaries.

Unsteady solutions of cavity flow were obtained using the time-dependent, explicit, two-step predictor-corrector finite algorithm of MacCormack.[11] The predictor and corrector steps can be written as

$$\overline{U_{i,j}^{n+1}} = U_{i,j}^n - \frac{\Delta t}{\Delta \xi}(E_{i+1,j}^n - E_{i,j}^n) - \frac{\Delta t}{\Delta \eta}(F_{i,j+1}^n - F_{i,j}^n) \quad (25)$$

$$U_{i,j}^{n+1} = \frac{1}{2}\left[U_{i,j}^n + \overline{U_{i,j}^{n+1}} - \frac{\Delta t}{\Delta \xi}(\overline{E_{i,j}^{n+1}} - \overline{E_{i-1,j}^{n+1}}) - \frac{\Delta t}{\Delta \eta}(\overline{F_{i,j}^{n+1}} - \overline{F_{i,j-1}^{n+1}})\right] \quad (26)$$

where the superscripts n, $n + 1$ denote the time levels, and the overbar denotes predictor values. As part of the algorithm, a fourth-order pressure damping term,[12] commonly employed to suppress numerical oscillations arising from the regions with large gradients, was added at each predictor and corrector step.

Results and Discussion

Although numerical solutions of cavity flow exist,[8,10,13] there are no numerical solutions for the cavity flow with passive control. This paper provides the first numerical solutions of cavity flowfield with passive control. To validate the computational code, numerical solutions of an *open* and *closed* flow without passive control are first obtained. The results of the computations without passive control also provided a reference case for the passive-control computations. For the initial conditions of the computation, the upstream conditions are imposed for the flow outside the cavity, and inside the cavity the flow is assumed to be static. The freestream conditions and cavity specifications used for this study are listed in Table 1.

Open Cavity

After a visual inspection of the instantaneous results obtained by running the code for $30T_c$, where characteristic time T_c was defined as the time it would take for the freestream to move 1 in., it was considered that the nonphysical initialization of the flowfield was purged and that the flow had entered a self-sustained oscillatory state. Presented in Figs. 5 and 6 are the computed density contours of the flowfield and the velocity vectors within the cavity, respectively, at five instants of time during a cycle of oscillation. The density contours are normalized with respect to the freestream value. In Fig. 5, the shear layer is seen to be highly unsteady and constantly changes its shape and impingement location during

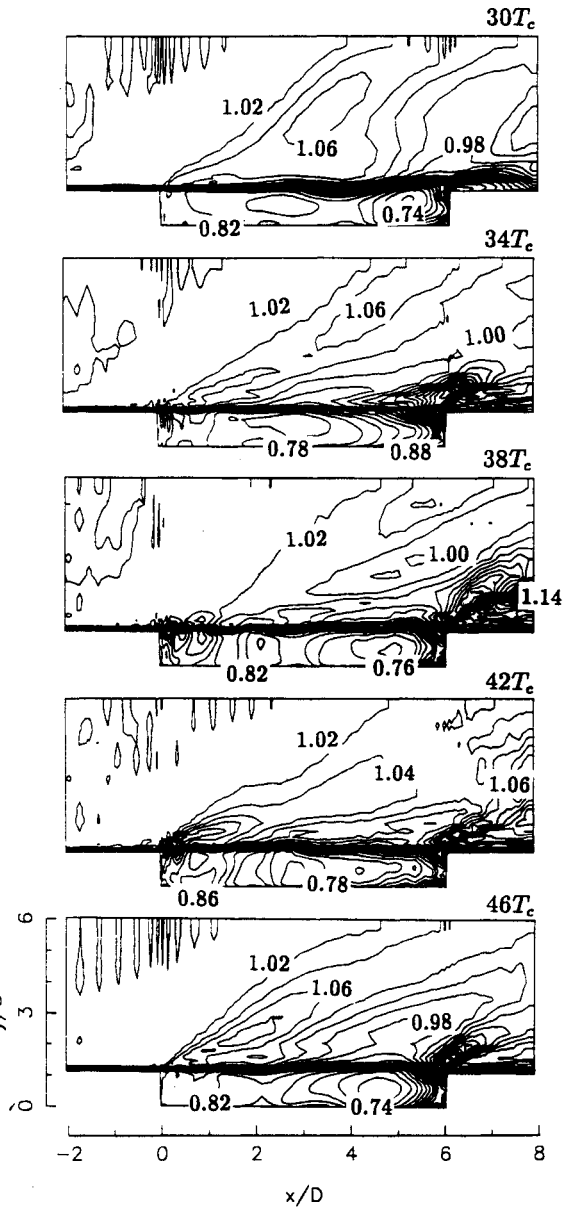

Fig. 5 Density contours for a cycle of oscillation.

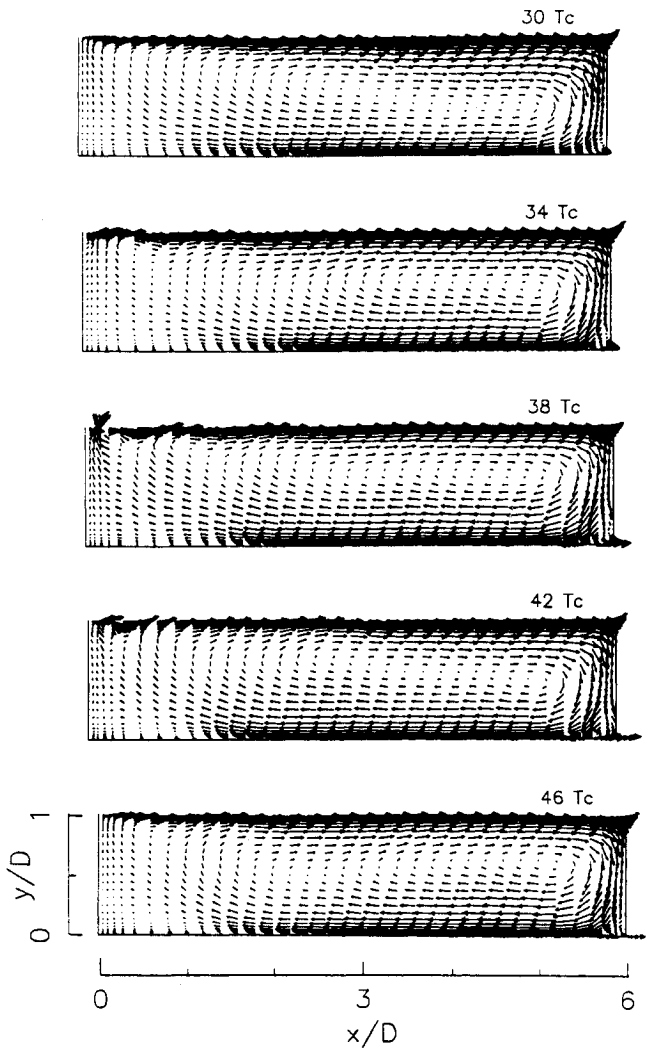

Fig. 6 Velocity vector plots within *open* cavity for a cycle of oscillation.

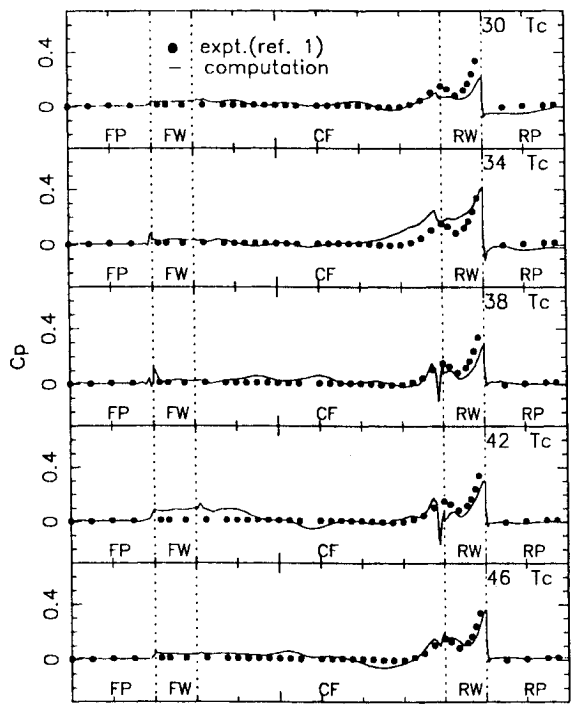

Fig. 7 Surface pressure coefficient distributions for a cycle of oscillation.

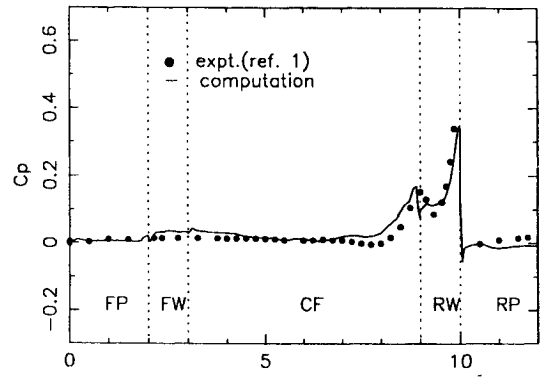

Fig. 8 Time-averaged surface pressure coefficient distribution.

the oscillation. In Fig. 6, the vortices driven by the shear layer are seen to continuously move around. It took approximately $20T_c$ for a complete cycle of flow oscillation. The flow oscillations in the next cycle were very similar but not exactly the same as the oscillations in the previous cycle. The sequence of instantaneous surface pressure coefficients corresponding to the previous plots is shown in Fig. 7; since no experimental unsteady pressures were available, the time-averaged surface pressure is shown for comparative purposes. The computed surface pressure is seen to undergo severe fluctuations during a cycle of oscillation depending upon the location and strength of the vortices. The computed surface pressure averaged over a cycle of oscillation is compared with the experiment in Fig. 8. In general, excellent agreement is shown between the computed and experimental data, with only a small discrepancy at the location of the shear-layer impingement on the rearward cavity wall. The computed drag coefficient, obtained by integrating the pressures on the forward and rearward walls of the cavity, was determined to be 0.13.

Closed Cavity

Unlike the *open* cavity flow, no significant flow fluctuations were detected in the *closed* flow computation. Figure 9 shows the computed density contours. A strong expansion fan is seen near the upstream corner of the cavity, where the shear layer is turned towards the cavity floor; strong compression waves are formed at the shear-layer impingement and separation locations on the cavity floor. Clockwise rotating vortices are formed in the separated flow regions near the forward and rearward walls of the cavity, as seen in the velocity vectors plot (Fig. 10). Within much of the cavity the velocities are comparable to the freestream velocity. The computed and experimental pressure coefficient distribution (Fig. 11) shows a low pressure on the forward wall due to the initial expansion; a rise in pressure at the shear-layer impingement region followed by a relatively uniform pressure in the region where the shear layer is attached to the cavity floor; and then an increasing pressure as the shear layer detaches from the cavity floor and exits the cavity at the rearward wall. The computed pressure coefficients are underpredicted near the forward wall, and overpredicted near the rearward wall. The major source of this discrepancy is believed to be the three-dimensional effects in the experiment; that is, the experiment is three-dimensional (cavity width, $W/D = 5.5$) and the computation is two-dimensional (i.e., infinitely wide cavity). For *closed* cavity computations, it is believed that with the wider cavities, the shear layer expands more freely, resulting in a sharper flow deflection and lower pressure near the forward wall. With the stronger flow expansion, the flow inside the cavity becomes faster for a wider cavity, and this faster flow inside the cavity inevitably ends up with a stronger exit shock, causing the higher pressure rise. A similar three-dimensional effect on the cavity surface pressure distribution was also observed in the surface pressure measurements of transitional cavities ($10 < L/D < 13$) with various widths and these three-dimen-

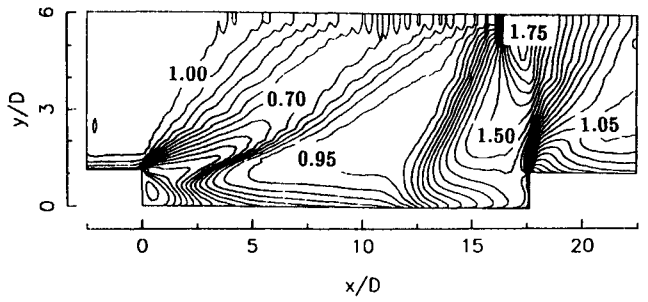

Fig. 9 Density of contour of *closed* cavity.

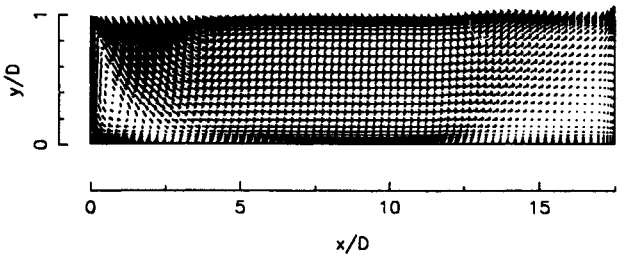

Fig. 10 Velocity vector plot within *closed* cavity.

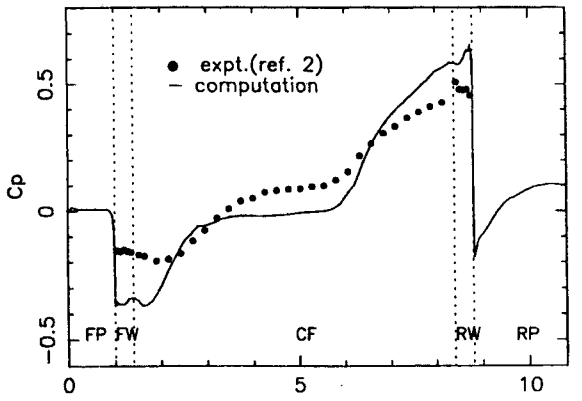

Fig. 11 Surface pressure coefficient distribution of *closed* cavity.

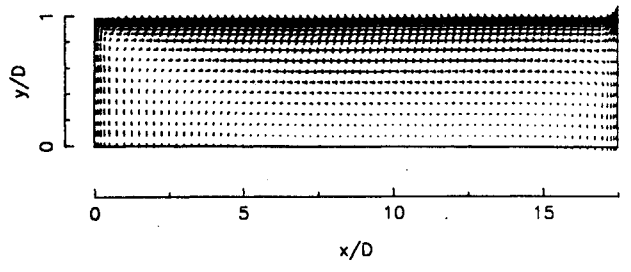

Fig. 12 Velocity vector plot within *closed* cavity with passive control.

sional effects are experimentally found to be much greater for a *closed* cavity than *open* cavity.[1] This explains why the *closed* cavity computation shows just qualitative agreement with the experiment, whereas the *open* cavity computation shows quantitative agreement with the experiment. The *closed* cavity drag coefficient was determined to be 0.95.

Closed Cavity with Passive Control

In Fig. 12, the velocity vectors of the *closed* cavity flow with passive control are shown; the passive venting system is seen to dramatically change the flow within the cavity. The separated flow regions that were observed near the forward and rearward walls in the *closed* cavity without passive control are seen to be absent; the flow velocities within the cavity are substantially lower than the freestream values. This passive control allowed air from the high-pressure region at the rear

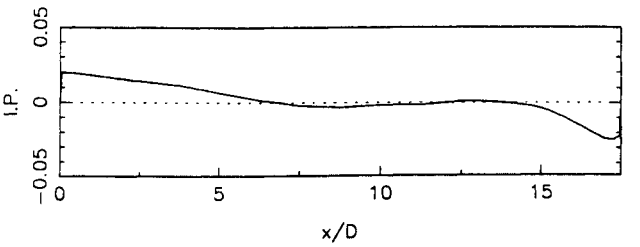

Fig. 13 Injection parameter on porous floor of *closed* cavity with passive control.

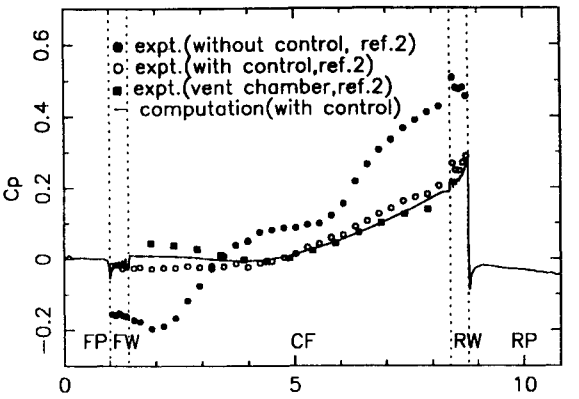

Fig. 14 Surface pressure coefficient distribution of *closed* cavity with passive control.

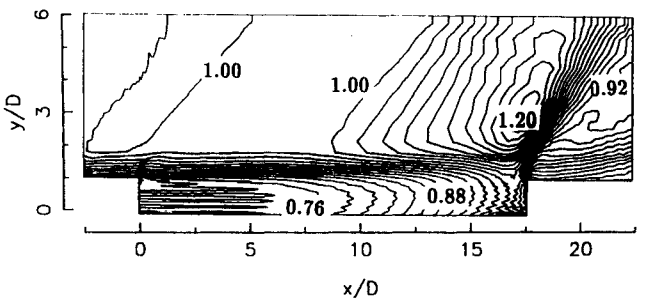

Fig. 15 Density contour of *closed* cavity with passive control.

of the cavity to vent to the forward of the cavity; a large circulation flow region within the cavity, centered at 60% of the cavity length measured from the forward wall of the cavity, is seen to be formed. The injection parameter, a measure of the local mass flux injected or withdrawn from the porous cavity floor, is shown in Fig. 13; this result shows that the normal wall velocities are small, typically less than 5% of the freestream velocity. It is interesting to notice that there is only negligible mass transfer over 40% of the cavity floor located around the center of circulation, suggesting that other methods such as ducts installed on the cavity floor could indeed be used to transport air from the high-pressure region at the rear of the cavity to the low-pressure region at the front part of the cavity. The computed surface pressure distribution is shown in Fig. 14; also shown by the filled-square symbols is the experimental vent chamber pressure. The features of the surface pressure distribution are quite similar to that of an *open* cavity flow—namely, a nearly constant pressure over the forward portion of the cavity floor followed by a gradual pressure increase over the near portion. The experimentally measured surface pressure with and without passive control are also shown by the unfilled and filled-circle symbols, respectively. The computed surface pressure distribution agrees very favorably with the experimentally measured surface pressure; this result confirms that the simulation of the passive control by the use of a linear form of the Darcy pressure-velocity law is appropriate for cavity flows. The result also shows that the three-dimensional effects of a *closed* cavity are

minimized by applying the passive control. The density contour plot is shown in Fig. 15. Consistent with the pressure distribution, there are no expansion waves near the forward wall, and most of the shear layer bridges the cavity. The overall flowfield characteristics of an *open* cavity flow and *closed* cavity flow with passive control are similar, but the shear-layer structure of a *closed* cavity flow with passive control is slightly different from that of an *open* cavity flow; namely, in the former flow, a portion of the shear layer separates from the main shear flow and weakly impinges on the floor. This action caused the pressure on the floor to start to increase in the middle of the floor for the *closed* cavity with passive control, whereas the same increase occurred near the rearward wall of the cavity for *open* flow. With this flowfield change, the computed drag coefficient of this *closed* cavity with passive control was determined to be 0.25.

Another interesting point is that even though the surface pressure distribution of a *closed* flow with passive control is smaller to that of an *open* flow, the large surface pressure fluctuations associated with the *open* cavity flow did not exist in the *closed* flow with passive control. Although disturbances are generated at the shear layer separation location, these are apparently damped by viscous dissipation effects in the shear layer. Further work is being conducted to examine the passive effect in the unsteady cavity flowfields.

Conclusions

Time-accurate solutions for supersonic flow over cavities were obtained by numerically solving the unsteady Navier-Stokes equations. The Navier-Stokes code was first validated by calculations of *open* and *closed* cavity flows, and then the capability of the numerical scheme to predict cavity flow with passive control was demonstrated. Simulation of the flow over an *open* cavity ($L/D = 6$) showed that this flow undergoes severe fluctuations and the time-averaged surface pressure distribution agreed quite well with the experimental measurements. No significant flow fluctuations were detected in the *closed* cavity ($L/D = 17.5$) computation, and the numerical solution showed just qualitative agreements with experimental data mainly due to the three-dimensional effects, which are observed to be much greater for a *closed* cavity than *open* cavity. The simulation of a flow over a cavity with passive control ($L/D = 17.5$) was conducted with the use of a linear Darcy pressure-velocity law. The following are significant findings observed in the study of the passive control applied to the *closed* cavity:

1) Passive control modifies the flowfield of a *closed* cavity to nearly that of an *open* cavity. The strong expansion and compression waves detected in the *closed* cavity flowfield are absent with the passive control.

2) Passive control caused a large circulation flow region centered at 60% of the cavity length from the forward face of the cavity to be formed, instead of the two clockwise vortices in the *closed* cavity without passive control.

3) The velocity of fluid injected or withdrawn from the porous surface was small, less than 5% of the freestream velocity. Also this mass transfer was negligible over the 40% of the porous surface.

4) By applying the passive control, the computed drag coefficient of the *closed* cavity was reduced by a factor of 4, from 0.95 (without passive control) to 0.25 (with passive control).

5) Although the flowfield of a *closed* cavity with passive control mimics the *open* cavity flowfield, it appears that no large flow fluctuations associated with the *open* cavity flowfield exist in the *closed* cavity flowfield with passive control.

The results of these first numerical studies of passive control applied to *closed* cavity have shown to be very promising. Work is continuing to examine in detail the unsteady flow features of the cavity flowfield with passive control.

Acknowledgments

The authors are grateful to Floyd Wilcox, NASA Langley Research Center, for providing tabulated copies of his experimental data, and useful discussions concerning the experiments. NASA Langley Research Center provided some computational facilities for the computations. A substantial portion of the calculations were conducted on the North Carolina Supercomputing Center Cray Y-MP. This work was supported in part by the North Carolina Board of Science and Technology under Grant 90SE03 and in part by the NASA Cooperative agreement Grant NCC1-46.

References

[1]Stallings, R. L., Jr., and Wilcox, F. J., "Experimental Cavity Pressure Distributions at Supersonic Speeds," NASA TP-2683, June 1987.

[2]Wilcox, F. J., "Passive Venting System for Modifying Cavity Flowfields at Supersonic Speeds," *AIAA Journal*, Vol. 20, March 1988, pp. 374–376.

[3]Chokani, N., and Squire, L. C., "Passive Control of Shock/Boundary Layer Interactions: Numerical and Experimental Studies," *Proceedings of the Symposium Transsonicum III*, International Union of Theoretical and Applied Mechanics, Gottingen, Germany, 1989, pp. 24–27.

[4]Savu, G., Trifu, O., and Dumitrescu, L. Z., "Suppression of Shocks on Transonic Airfoils," *Proceedings of 14th International Symposium of Shock Tubes & Shock Waves*, Sydney, Australia, 1983, pp. 92–101.

[5]Delery, J. M., "Shock Wave/Turbulent Boundary-Layer Interaction and its Control," *Progress in Aerospace Sciences*, Vol. 22, No. 2, 1985, pp. 209–280.

[6]Thiede, P., Krogmann, P., and Stanewsky, E., "Active and Passive Shock/Boundary Layer Interaction Control on Supercritical Airfoils," AGARD CP-365, May 1984.

[7]Bahi, L., Ross, J. M., and Nagamatsu, H. T., "Passive Shock Wave/Boundary Layer Control for Transonic Airfoil Drag Reduction," AIAA Paper 83-0137, Jan. 1983.

[8]Rizzetta, D. P., "Numerical Simulation of Supersonic Flow Over a Three-Dimensional Cavity," *AIAA Journal*, Vol. 26, July 1988, pp. 799–807.

[9]Wakiewicz, J. D., Shang, J. S., and Hankey, W. L., "Numerical Simulation of Near Wakes Utilizing a Relaxation Turbulence Model," *AIAA Journal*, Vol. 18, Dec. 1980, pp. 1440–1445.

[10]Hankey, W. L., and Shang, J. S., "Analyses of Pressure Oscillations in an Open Cavity," *AIAA Journal*, Vol. 18, Aug. 1980, pp. 892–898.

[11]MacCormack, R. W., "The Effect of Viscosity in Hypervelocity Impact Cratering," AIAA Paper 69-354, April 1969.

[12]MacCormack, R. W., and Baldwin, B. S., "A Numerical Method for Solving the Navier-Stokes Equations with Application to Shock-Boundary Layer Interaction," AIAA Paper 75-1, Jan. 1975.

[13]Baysal, O., Srinivasan, S., and Stallings, R. L., Jr., "Unsteady Viscous Calculations of Supersonic Flows Past Deep and Shallow Three-Dimensional Cavities," AIAA Paper 88-0101, Jan. 1988.